Original Paper

Electric Potential Response Characteristics and Constitutive Model of Coal Under Axial Static Load–Dynamic Load Coupling

Zesheng Zang,[1,2,3] **Zhonghui Li,**[1,2,3,7] **Enlai Zhao,**[1,2,3] **Xiangguo Kong,**[6] **Yue Niu,**[4,5] **and Shan Yin**[1,2,3]

The electrical and magnetic signals generated by coal fracture can expose the mechanical properties and fracture behavior of coal, which are of great significance for underground mining engineering safety under high static stress and dynamic load disturbance conditions. This work used the split Hopkinson pressure bar experimental apparatus to perform impact dynamic experiments on coal samples with axial static load–dynamic load coupling and test the electric potential (EP) signal. We studied the characteristics of coal's EP response under various dynamic and static load coupling conditions, discussed the mechanisms by which different variables affected EP response, and built an EP-based constitutive model of coal damage progression. The results revealed that under the coupling of axial static load–dynamic load, noticeable EP signals are stimulated in coal, and the change in EP signal is well correlated with the change in mechanical behavior. However, increasing dynamic load can excite a greater EP signal, and the peak EP grows linearly with stress. Peak EP first increases linearly as the axial static load increases, and when the axial static load reaches the critical threshold, peak EP and peak stress start to decrease progressively. Peak EP variation well corresponds to peak stress. Crack propagation and free electron escape can explain the effect of axial static load and dynamic load on coal EP signal at the micro level. On this basis, we developed an EP constitutive model of coal damage evolution under axial static load–dynamic load coupling. The model can well calculate the stress state of coal. The study's findings provide a solid theoretical foundation for security monitoring of deep-underground engineering.

KEY WORDS: SHPB, EP response, Mechanical behavior, Micro mechanism, Constitutive model.

---

[1]National Engineering Research Center for Coal Gas Control, China University of Mining and Technology, Xuzhou 221116, Jiangsu, China.
[2]Key Laboratory of Gas and Fire Control for Coal Mines of Ministry of Education, China University of Mining and Technology, Xuzhou 221116, Jiangsu, China.
[3]School of Safety Engineering, China University of Mining and Technology, Xuzhou 221116, Jiangsu, China.
[4]State Key Laboratory for GeoMechanics and Deep Underground Engineering, China University of Mining and Technol-

ogy, Xuzhou 221116, Jiangsu, China.
[5]Frontier Scientific Research Center of Fluidized Mining of Deep Resources, China University of Mining and Technology, Xuzhou 221116, Jiangsu, China.
[6]College of Safety Science and Engineering, Xian University of Science and Technology, Xian 710054, Shaanxi, China.
[7]To whom correspondence should be addressed; e-mail: leezhonghui@163.com

INTRODUCTION

Shallow mineral resources are depleted rapidly due to the rising demand for resources and energy, and many underground projects are shifting gradually to deeper levels. The geological conditions for underground engineering are more complex and demanding (He et al. 2018; Li et al. 2021a, 2023; Kong et al. 2022; Liu et al. 2023). Coal under high static stress is disturbed frequently by dynamic loads. High static stress can be in-situ stress, such as gravity or tectonic stress (Li et al. 2021b; Feng et al. 2022). Dynamic loads disturbances may include earthquakes, digging, and blasting (Kenkmann et al. 2014; Liu et al. 2018; Zhang et al. 2020; Jiang et al. 2021; Ji et al. 2023). Under high static stress and dynamic load coupling at high loading rates, such frequent risks cause considerable fractures of coal seams (Cai et al. 2007; Dai & Xia 2013; Xia & Yao 2015; Li et al. 2020a). The mechanical behavior and fracture mode of coal under dynamic load are different from those under single static load, which poses further challenges to forecast coal failure process under extreme circumstances.

The SHPB (split Hopkinson pressure bar) is a standard kinetic test equipment (Zhou et al. 2012) that may mimic dynamic load issues in subterranean engineering in addition to testing the dynamic behavior of coal at high strain rates. There are previous studies on various underground materials (coal, rock, and concrete, for example) under various loading circumstances, including single dynamic loading experiments (Dai et al. 2010; Li et al. 2021c; Padmanabha et al. 2021; Zang et al. 2021; Zhang et al. 2022a, 2022b), axial static–dynamic coupling loading experiments (Enomoto & Hashimoto 1990; Weng et al. 2018; Li et al. 2020b), and triaxial impact experiments (Gong et al. 2019; Kong et al. 2020, 2021; Gu et al. 2023). The results of those studies showed that the fracture process of coal rock under the coupling of axial static load and dynamic load has significant dynamic characteristics. With increase in strain rate, the dynamic strength and peak strain of the specimen will increase. The dynamic behavior of a specimen shows strong dependence on strain rate. The axial static load can improve the strength of a coal sample to a certain extent, resulting in higher resistance of the coal sample. These research results have laid a solid foundation for the research of this paper.

The difference in kinetic properties is essentially a reflection of the different mechanisms of change in the internal microstructure of a material (Howe & Greb 2005). Primary cracks in the field coal are rich, and the deformation and failure of coal are a result of internal microcrack penetration and propagation, and so the evolution law of coal surface cracks can, to some extent, reflect the alteration of its interior microstructure (Li et al. 2019a; Liu et al. 2020; Zhang et al. 2022a, 2022b). Therefore, high-speed photography technology, which has been extensively used in dynamic load testing, is utilized in this experiment's non-destructive testing techniques, which can help to understand in detail the crack propagation and fragment ejection phenomenon in the coal fracture process.

Numerous laboratory investigations have demonstrated that loading coal rock externally generates significant electric potential (EP) signals (Freund 2002; Takeuchi et al. 2006; Vallianatos & Triantis 2008; Scoville et al. 2015). EP signals are a wide concern in seismology, geophysics, geological engineering and underground engineering. Detecting EP signals holds promise for monitoring stress and fracture of coal rock and it can be used to foresee dynamic coal rock disasters. EP signals are produced by mechanisms like charge separation during coal rock deformation and fracture (Enomoto & Hashimoto 1990; Slifkin 1993; Surkov et al. 2003; Stavrakas et al. 2004; Freund 2011; Leeman et al. 2014), and they carry rich coal fracture information. The evolution of time series features (e.g., EP amplitude, cumulative charge, spatial distribution) of EP signals, which are closely related to the mode and seriousness of coal fracture, can shed light on the deformation and failure process of coal. This aids in monitoring coal's stability (Li et al. 2019c; Zhang et al. 2021). In general, large-scale fractures typically result in greater amplitude EP signals (Niu et al. 2022). In the literature (Kyriazopoulos et al. 2005; Triantis et al. 2006, 2007; Stergiopoulos et al. 2015; Li et al. 2021d), uniaxial compression, Brazilian splitting, three-point bending, and triaxial tests were used to study the EP response characteristics of coal rock under various stress circumstances. The study's results support the aforementioned viewpoints and arrive at a universal conclusion. In uniaxial test circumstances, a coal damage evolution model based on EP signal is established (Yin et al. 2017). Subsequently, the model is enhanced further by considering the coupling effect of gas and stress (Niu et al. 2019). Therefore, EP testing, a geophysical approach, is a promising way to help predict engineering geological disasters.

Figure 1. Specimens of coal.

Figure 2. Semi-quantitative X-ray diffraction of the studied coal.

However, prior researches were primarily conducted under quasi-static stress circumstances, and a sample's fracture process was quite sluggish. Coal is more intensely affected by high strain rate dynamic loads in terms of failure strength, fracture mode, and energy conversion. The EP response characteristics and generating mechanism are also considerably distinct (Zhang & Zhao 2014). At present, there is lack of research on EP response characteristics and EP constitutive model of coal under dynamic load.

Therefore, coal was the research subject for this work, which also made use of axial static load and dynamic load coupling loading impact dynamics experiments, and synchronous acquisition EP signals. Under diverse dynamic and static loads, the coal's EP response characteristics were studied, and the effects of axial static load and dynamic load on the EP response law were deeply analyzed. A constitutive model of coal damage evolution based on EP characterization was established taking the aforementioned factors into consideration.

EXPERIMENTS

Specimen Preparation

Specimens of coal was retrieved from the autonomous region of Inner Mongolia. This coal is hard and with few pores. The ZBL-U5200 nonmetallic ultrasonic detector was used to test the p-wave velocity of the specimens in order to guarantee that all of the specimens were similar, and the specimens with the smallest wave velocity difference were chosen for the experiment (Fig. 1). The coal's composition was determined by semi-quantitative X-ray diffraction to be 20.7% quartz, 9.9% albite,
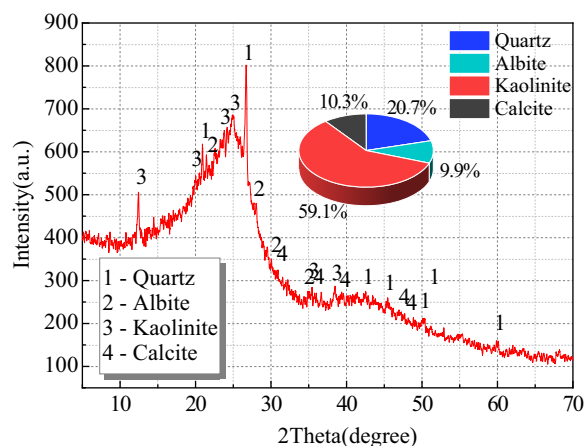
59.1% kaolinite, and 10.3% calcite (Fig. 2). To create a standard sample with diameter of 100 mm and height of 50 mm, coal was extracted from the same block and drilled in the same direction. A specimen's ends were then polished and ground to guarantee that the flatness was less than 0.02 mm in accordance with the guidelines established by the International Society for Rock Mechanics (ISRM) (Zhou et al. 2012). Table 1 displays the fundamental physical parameters of the specimens.

Experimental Setup

Using a conventional SHPB system, the dynamic compression experiment was conducted on the coal specimens, and a high-speed camera and EP signals were tested simultaneously. The SHPB is composed up of a high-pressure gas chamber, an impact bar, an incidence bar, a transmission bar, an infrared velocimeter, a damper, and an ultra-dynamic strain acquisition device (Fig. 3). The compression bar had a diameter of 100 mm, while the impact bar, incident bar, and transmitted bar had lengths of 400 mm, 5000 mm, and 3000 mm, respectively. The longitudinal wave velocity was 5100 m/s, the Young's modulus was 210 GPa, and the density was 2.7 g/cm^3. The EP acquisition system was composed up of a host, an acquisition card, wires, and electrodes. The COBWEB-DAU multi-channel acquisition instrument was used in the EP acquisition instrument. The test instrument had 12 monitoring channels, and a single channel had a frequency of 192 Hz–100 kHz. DC coupling and

Table 1. Fundamental physical parameters of coal samples

Specimen	Density (g/cm^3)	P-wave velocity (km/s)	Young's modulus (GPa)	Uniaxial compressive strength (MPa)
Coal	1.28	1.35	3.12	15.6
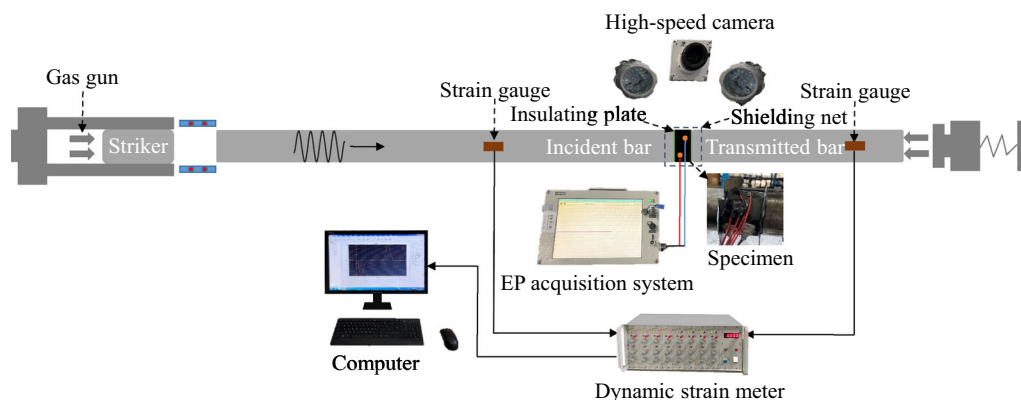
Figure 3. Experimental system.

multi-channel parallel acquisition were adopted, and the input impedance was 1 Ω. The electrode was made of copper electrode, and the conductivity was enhanced by coupling the conductive paste with the sample. The electrode collected the EP signals, which then traveled to the pre-converter for ''analog to digital'' conversion and, finally, the host for real-time display and recording. Phantom series high-speed cameras from VRI, USA, were used by the high-speed camera for parameter configuration and image acquisition with the corresponding Phantom Camera Control Application software. The system was composed mainly of high-speed camera, light source and computer. The shooting window was set to 521 × 256, and the number of frames per second was 48000.

Experimental Scheme

This experiment set various impact velocities and various axial static load settings for dynamic uniaxial compression trials in order to study the EP response characteristics of coal under various dynamic and static load coupling. The specimens D-1 through D-5 were tested at various impact velocities, which were set to 1 m/s, 3 m/s, 5 m/s, 7 m/s, 9 m/s,

and the corresponding strain rates were 49.05 s^{-1}, 70.46 s^{-1}, 144.21 s^{-1}, 192.54 s^{-1}, 272.56 s^{-1}, respectively, with the axial static load being 3 MPa. The specimens S-1 through S-4 were tested at various axial static loads, which were 1 MPa, 5 MPa, 7 MPa, and 9 MPa, respectively, with strain rate of 190 s^{-1}. The experiment was designed to obtain the effects of various dynamic and static loads on the EP response properties of coal fracture and to reveal the mechanism by which coal EP signal responds to various dynamic and static stresses.

Experimental Principle

The one-dimensional stress wave hypothesis and the homogeneity hypothesis must be satisfied by the SHPB experiment. The ''three-wave method'' was used to process the data if the specimen achieved dynamic stress balance during the experiment. The stress wave signal acquired by the acquisition card was separated to extract the incident wave $\varepsilon_{In.}(t)$, reflected wave $\varepsilon_{Re.}(t)$, and transmitted wave $\varepsilon_{Tr.}(t)$. The strain rate $\dot{\varepsilon}(t)$, strain $\varepsilon(t)$, and stress $\sigma(t)$ of a specimen were derived as follows according to the assumption of a one-dimensional stress wave(Li et al. 2000; Zhang & Zhao 2014):

$$\dot{\varepsilon}(t) = \frac{c}{L_0}[\varepsilon_{In.}(t) - \varepsilon_{Re.}(t) - \varepsilon_{Tr.}(t)] \quad (1)$$

$$\varepsilon(t) = -\frac{c}{L_0}\int_0^t [\varepsilon_{Re.}(t) + \varepsilon_{Tr.}(t) - \varepsilon_{In.}(t)]dt \quad (2)$$

$$\sigma(t) = \frac{A}{2A_0}E[\varepsilon_{In.}(t) + \varepsilon_{Re.}(t) + \varepsilon_{Tr.}(t)] \quad (3)$$

where c represents the propagation speed of the stress wave in the elastic bar, which was 5100 m/s; L_0 is length of a sample, which was 100 mm; E is the elastic modulus (210 GPa) of the elastic bar; A is the cross-sectional area of the elastic bar; A_0 is the cross-sectional area of a sample; t is the stress wave pulse duration.

Dynamic Stress Equilibrium Test

The typical pulse waveforms gathered by the strain acquisition apparatus are shown in Figure 4a and b. A gradually rising half-sine incident wave was produced in the incident bar as a result of the impact of the impact bar, and the waveforms of all specimens had similar shapes. For experimental results to guarantee accurate during dynamic compression, particularly before cracks appear, dynamic stress balancing was necessary (Li et al. 2019b). The dynamic stress balance of the experimental data must therefore be verified. The stress equilibrium curves of D-1-1 and S-1-1 are shown in Figure 4c and d. The superposition of the incident wave stress curve and the reflected wave stress curve was shown to be highly coincident with the transmission wave stress curve in the figure, indicating that the dynamic stress balance was attained and, thus, the reliability of the experimental findings.

RESULTS

Dynamic Stress–Strain Curve

The dynamic stress–strain curves of the specimens under diverse dynamic and static load situations are depicted in Figure 5, and the associated mechanical parameters are listed in Table 2. This paper only chose the data for sample number 1 for analysis because the mechanical properties of the specimens were nearly identical under the same circumstances. Figure 5 demonstrates that the com-

paction stage of the stress–strain curve of the specimen was very short and, that at the early stage of loading, it soon reached the linear elastic stage. This is because the specimen compacted quickly under a dynamic load with high strain rate. Additionally, the specimen had a pre-axial static load, closed internal primary microcracks, and it had been in a dense state overall. Therefore, the specimen moved swiftly into the stage of linear elastic. The specimen primarily experienced recoverable elastic deformation during the linear elastic stage (stage II), and the stress increased roughly linearly with increase in strain. The sample entered the plastic deformation stage when the stress reached between 70 and 80% of the peak stress (stage III). At this stage, the sample's strain kept growing, but the rate at which stress was increasing slowed down and the curve became nonlinear. This was because the sample started to fracture plastically when the external load grew gradually to the critical value, microcracks began to develop and the stress in the fracture region was released. Microcracks continued to grow and penetrated beyond the peak stress (stage IV), and the major fracture then took place. The stress–strain curve showed 'rebound' phenomenon. The general consensus was that the release of elastic energy was what caused this occurrence.

The dynamic stress–strain curve of the samples exhibited significant strain rate sensitivity (Fig. 5a). The peak stress and peak strain of the sample rose synchronously as the strain rate rose, enhancing the sample's capacity to withstand external loads. Similar to this, the sample's peak stress and peak strain increased initially before decreasing as the axial static load was raised. The results showed that, within a certain threshold range, the axial static load can increase the sample's strength; nevertheless, beyond that critical point, it promoted the sample's failure.

Temporal Variation Characteristics of EP at Different Strain Rates

The time series features of the coal EP response at various strain rates are shown in Figure 6. The EP response was well associated with the stress of the specimen, and the EP change appeared to be dependent on the coal's fracture severity and stress intensity. Therefore, it was essential to thoroughly research the EP response characteristics of each stage of specimen damage.
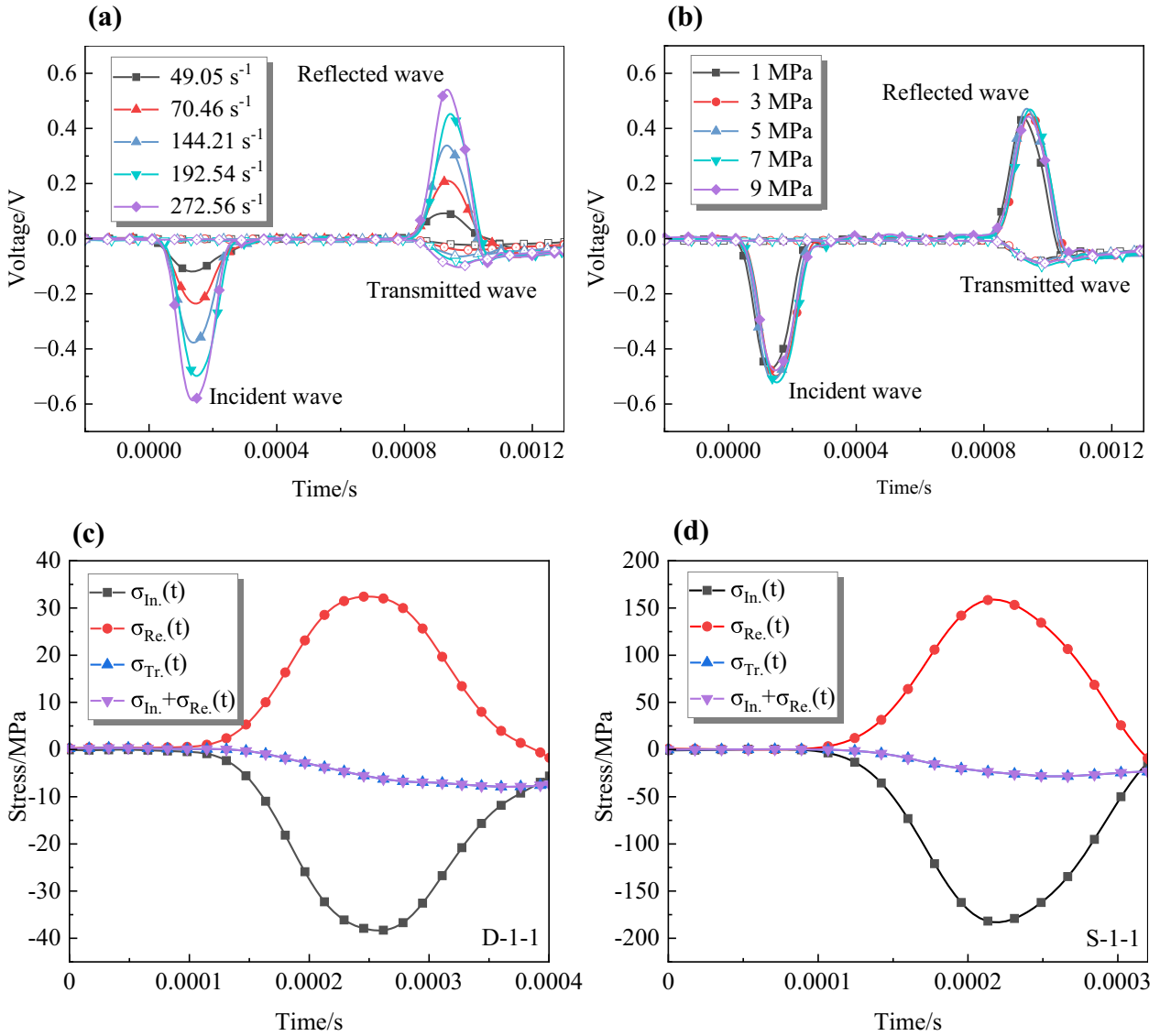
Figure 4. Typical stress wave and dynamic stress equilibrium of specimens.

Due to the low sample stress level in the initial stage of loading (stage I), the coal sample's original fracture can only be closed in the particle range. The EP signals often exhibited a low value state and only exhibited a little fluctuation. The coal sample then moved into the linear elastic stage (stage II). The EP rose linearly with stress at this stage. The coal sample was totally dense throughout this procedure, and its interior particles experienced recoverable offset displacement. The specimen experienced plastic deformation when the stress reached the critical level for crack propagation (stage III). The

initiation and propagation of microcracks resulted in an exponential rise in EP as well as a continuous acceleration in rate of increase. Figure 6a–e of the comparison analysis demonstrated that the growth rate of EP in the process of stress rose steadily with increase in strain rate. This demonstrates that the primary determinant of an EP growth was dynamic load. The specimen experienced its principal fracture when the stress reached its peak amount, and the interior microcracks quickly grew and penetrated. Numerous EP signals were generated by the crack spreading, the EP rose quickly, and the EP
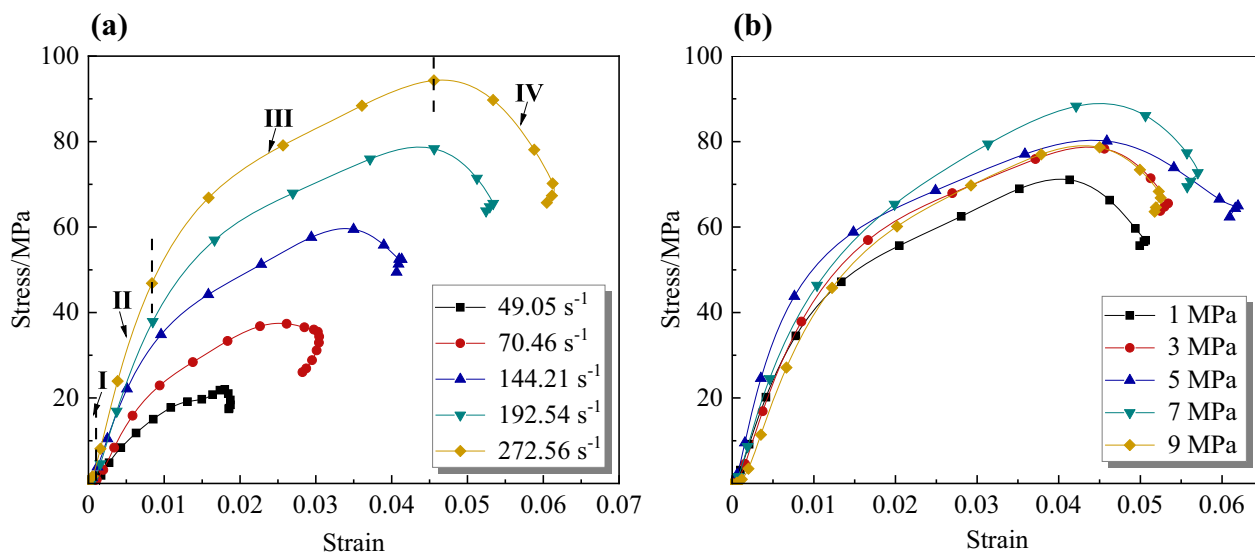
Figure 5. Stress–strain curves of (**a**) different strain rates and (**b**) different axial static loads.

Table 2. Experimental parameters of the tested specimens

| Sample no.	Impact velocity (m/s)	Axial static load (MPa)	Peak strength (MPa)		Elastic modulus (MPa)		Peak strain	
			Value	Average	Value	Average	Value	Average
D-1-1	1.19	3	22.05	21.82	1718	1711	0.0178	0.0174
D-1-2	1.05		21.47		1706		0.0172	
D-1-3	1.08		21.95		1711		0.0174	
D-2-1	3.12	3	37.46	36.23	2813	2764	0.0252	0.0243
D-2-2	3.04		36.02		2754		0.0241	
D-2-3	3.01		35.23		2725		0.0238	
D-3-1	5.04	3	59.63	59.32	3778	3775	0.0339	0.0337
D-3-2	4.98		56.29		3693		0.0321	
D-3-3	5.08		62.04		3854		0.0353	
D-4-1	6.96	3	78.71	80.14	4477	4587	0.0437	0.0442
D-4-2	7.04		80.21		4614		0.0442	
D-4-3	7.08		81.52		4671		0.0449	
D-5-1	8.75	3	94.39	98.6	5980	6134	0.0464	0.0491
D-5-2	8.88		99.43		6269		0.0498	
D-5-3	8.94		101.98		6154		0.0513	
S-1-1	6.79	1	71.19	73.21	4715	4829	0.0402	0.0418
S-1-2	6.85		73.53		4852		0.042	
S-1-3	6.89		74.93		4921		0.0433	
S-2-1	7.04	5	80.30	80.6	4680	4682	0.044	0.044
S-2-2	6.99		78.78		4545		0.0427	
S-2-3	7.08		82.72		4822		0.0453	
S-3-1	6.90	7	88.89	91.12	5039	5205	0.0445	0.0458
S-3-2	6.96		90.49		5195		0.0458	
S-3-3	7.02		93.98		5383		0.0472	
S-4-1	6.85	9	79.02	81.81	4396	4589	0.0430	0.0447
S-4-2	6.92		82.47		4601		0.0443	
S-4-3	6.96		83.94		4772		0.0468	
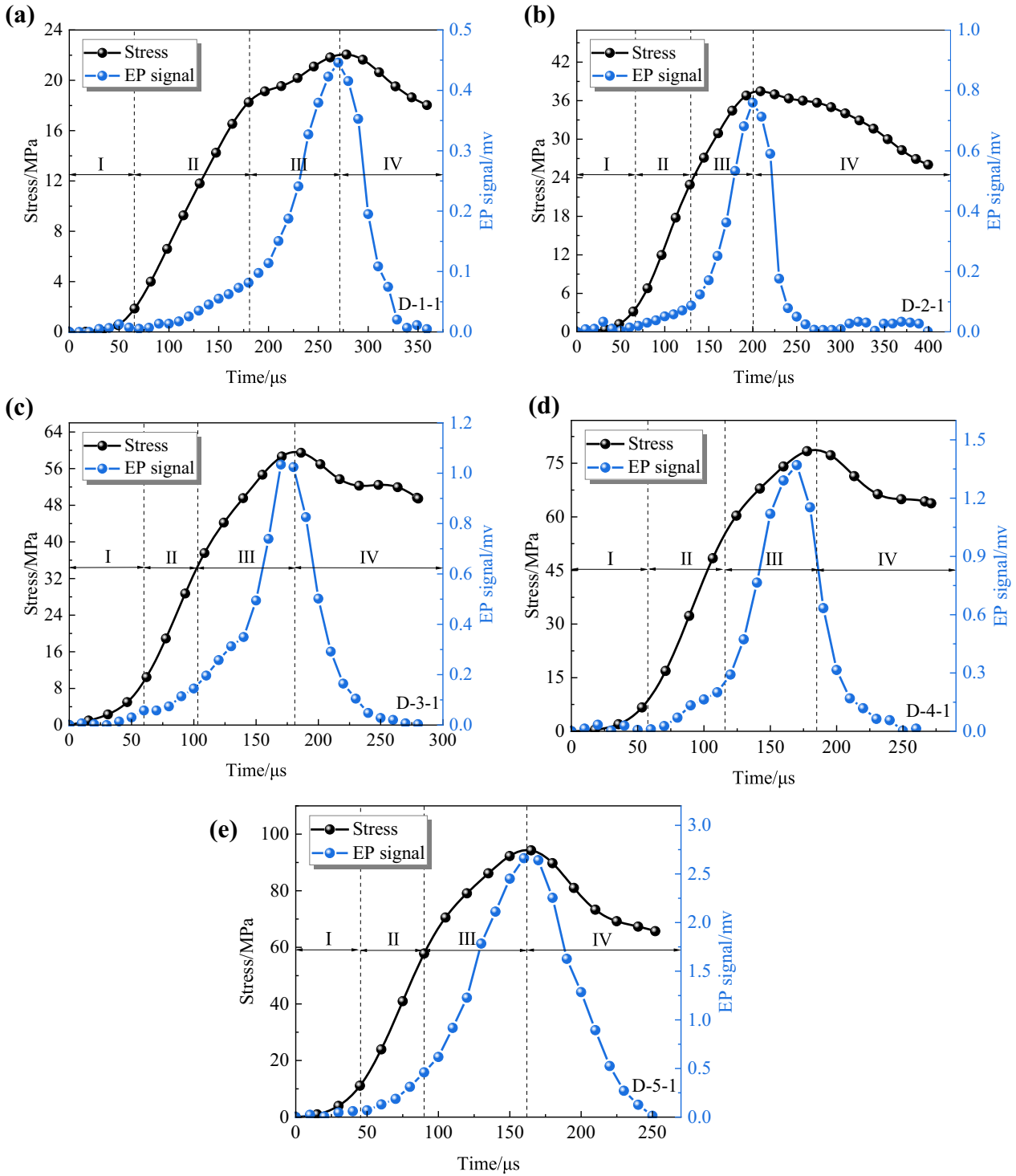
Figure 6. Time series variation of stress and EP of specimens with different strain rates: (**a**) D-1-1; (**b**) D-2-1; (**c**) D-3-1; (**d**) D-4-1; (**e**) D-5-1.

and stress peaked at the same time. When the specimen finally failed (stage IV), the EP slowly reduced as the stress diminished and eventually stabilized close to the zero scale line. It was necessary to quantify the relationship between EP response because they could reflect the coal fracture process.

The peak stress and peak EP variation curves with strain rate are shown in Figure 7a and b, respectively. These demonstrate the significant reliance of the sample's peak stress and peak EP on the dynamic load. Peak stress rose from 22.05 to 94.39 MPa as the strain rate rose from 49.05 to 272.56 s^{-1}, while peak EP rose from 0.44 to 2.66 mv. The fitting functions were:

$$S_p = 12.02 + 0.32r_i (R^2 = 0.96) \qquad (4)$$

$$V_p = 0.23 - 0.2 * \exp(r_i/111)(R^2 = 0.96) \qquad (5)$$

where S_p stands for peak stress, V_p for peak EP, and r_i for strain rate. The peak stress and peak EP of the specimen exhibited good linear and exponential fitting relationships with strain rate, respectively, according to the equations above, and the fitting coefficients were larger than 0.95. Figure 7c shows the fitting curve between the peak EP and the peak stress of the sample, and the fitting function was:

$$V_p = 0.57 + 0.01 * \exp(S_P/17.49)(R^2 = 0.94) \quad (6)$$

According to the above equation, the peak EP of the sample also showed an exponential growth trend with the increase of the peak stress, and the fitting coefficient was 0.94. It demonstrates that the existence of dynamic load can improve the dynamic strength of coal samples and enhance the ability of coal to resist damage. However, due to the complete destruction of the sample under dynamic load (only the sample D-1-1 was not destroyed completely), the failure process of the sample was more intense and could produce more cracks. The generated EP signal by the fracture of the coal sample increased gradually as the specimen failure process intensified. The peak EP and peak stress also showed good consistency.

Temporal Variation Characteristics of EP at Different Axial Static Loads

The time series characteristics of the coal EP response to various axial static stresses are shown in

Figure 8. According to the figure, the EP signal had response characteristics comparable to those mentioned previously. The coal sample was in the compaction stage at the beginning of the dynamic load, and the EP barely varied a little. Enter the linear elastic stage following, Figure 8a and b demonstrate that this stage increased linearly with stress, and the EP also exhibited a trend resembling a linear increase, which was consistent with the results presented above. It is interesting that neither Figure 8c nor Figure 8d showed a discernible rise in EP in this stage. This might be because when the axial static stress rose, the coal sample's elastic deformation became more pronounced. The specimen could more easily exceed the elastic deformation limit when subjected to dynamic load. The EP response produced by this process was therefore not remarkable. The specimen then quickly entered the plastic deformation stage, and the emergence and spread of microcracks also resulted in an exponential rise in EP. Similar to this, a quantitative analysis of the connection between EP and stress under varied axial static loads was conducted.

The peak stress and peak EP variation curves with axial static load are shown in Figure 9a and b, respectively. These figures show how the peak stress and peak EP of the coal sample were influenced significantly by the axial static load. The peak stress rose from 71.19 to 88.89 MPa and the peak EP rose from 0.91 to 1.92 mv, when the axial static load rose from 1 to 7 MPa. The peak stress then fell from 88.89 to 79.02 MPa, the peak EP from 1.92 to 1.58 mv, when the axial static load increased once more from 7 to 9 MPa. In the rising process, the variation of peak stress and peak EP with axial static load was fitted. The fitting functions were, respectively:

$$S_p = 68.84 + 2.73s_a (R^2 = 0.97) \qquad (7)$$

$$V_p = 0.78 + 0.15s_a (R^2 = 0.97) \qquad (8)$$

where s_a is axial static load. According to the above equations, the peak stress and peak EP of the sample exhibited a linear fitting relationship with the axial static load when the axial static load was low (1–7 MPa), and the fitting coefficient was 0.97. The peak stress and peak EP started to decline simultaneously when the axial static load exceeded the critical value, and their change trends were relatively similar. Figure 9c shows the fitting curve between the peak EP and the peak stress of the sample, and the fitting function was:
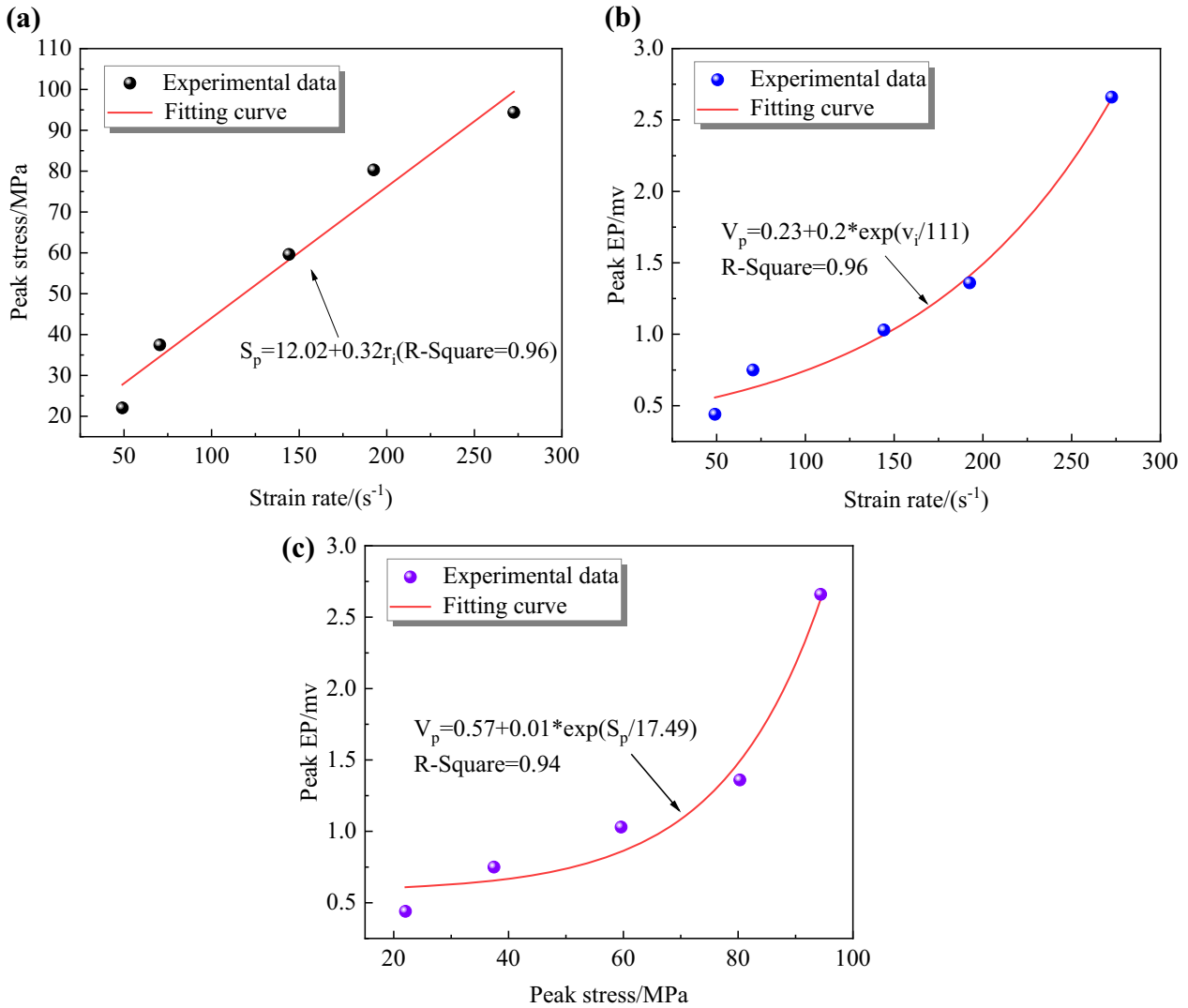
(a)

(b)

(c)

Figure 7. Relation of (**a**) peak stress and (**b**) peak EP to strain rates, and (**c**) peak EP to peak stress.

$$V_p = 2.91 - 32.83 * \exp(S_P/25.43)\left(R^2 = 0.89\right) \quad (9)$$

According to the above equation, the peak EP of the sample showed an exponential growth trend with increase in peak stress, and the fitting coefficient was 0.89. The change trend of the two also showed good consistency. This was due to the fact that under the influence of an axial static load, the coal's internal fractures gradually closed and became

denser. The dynamic strength of the specimen was enhanced by the application of an axial static stress. This process resulted in a constant accumulation of elastic energy inside the coal sample. The EP response was strengthened when the specimen broke because more elastic energy was released. Microcracks started to form in the coal sample as the axial static load went above the critical level, which encouraged the coal sample to fail and showed that
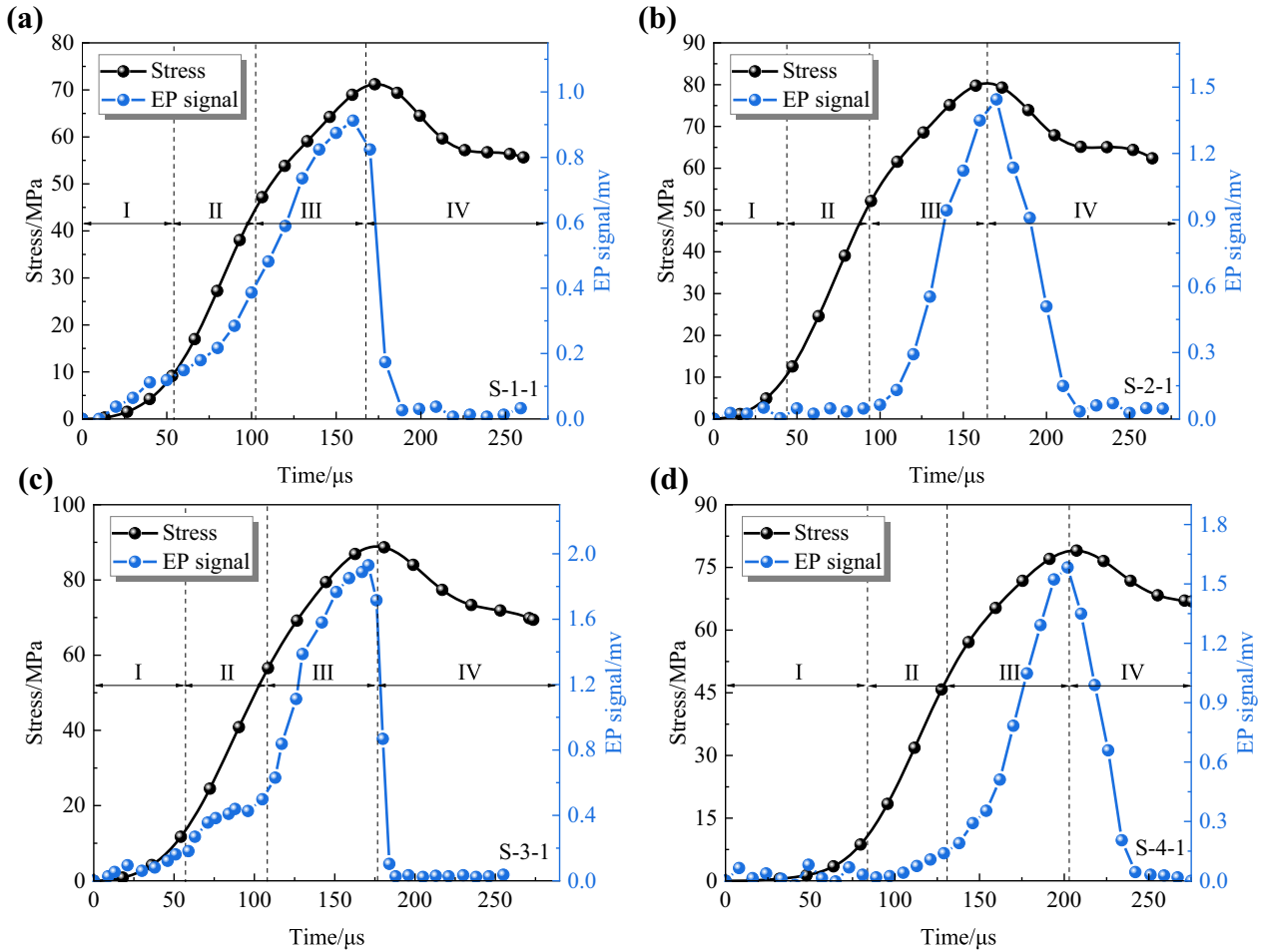
Figure 8. Time series variation of stress and EP of specimens with axial static loads: (**a**) S-1-1; (**b**) S-2-1; (**c**) S-3-1; (**d**) S-4-1.

the peak stress started to fall. A gradual reduction in the EP signal produced by the specimen under dynamic loading occurred as a result of the freshly formed microcracks consuming a portion of the elastic energy. This demonstrates that the creation of EP signals can reflect the sample's state of stress and failure process. Therefore, we conducted an in-depth analysis how EP coal signals are generated at various stages of dynamic load.

DISCUSSION

EP Generation of Coal Under Dynamic Loading

The physical foundation of an EP response is the creation of a free charge. Diverse fracture modes result in different sources of free charge because the

source of free charge in the coal rupture process is complex. For the quantitative relationship between coal deformation and free charge under dynamic load to be analyzed further, from the beginning time t_0 through a specific time t, the cumulative charge released from the specimen was expressed as:

$$Q_t \propto \int_{t_0}^{t} U(t)\mathrm{dt} \qquad (10)$$

where Q_t is the accumulated charge at time t, and $U(t)$ is the EP value at time t. The calculated values were normalized, and the normalization was:

$$Q_n = \frac{Q_t - Q_i}{Q_m - Q_i} \qquad (11)$$

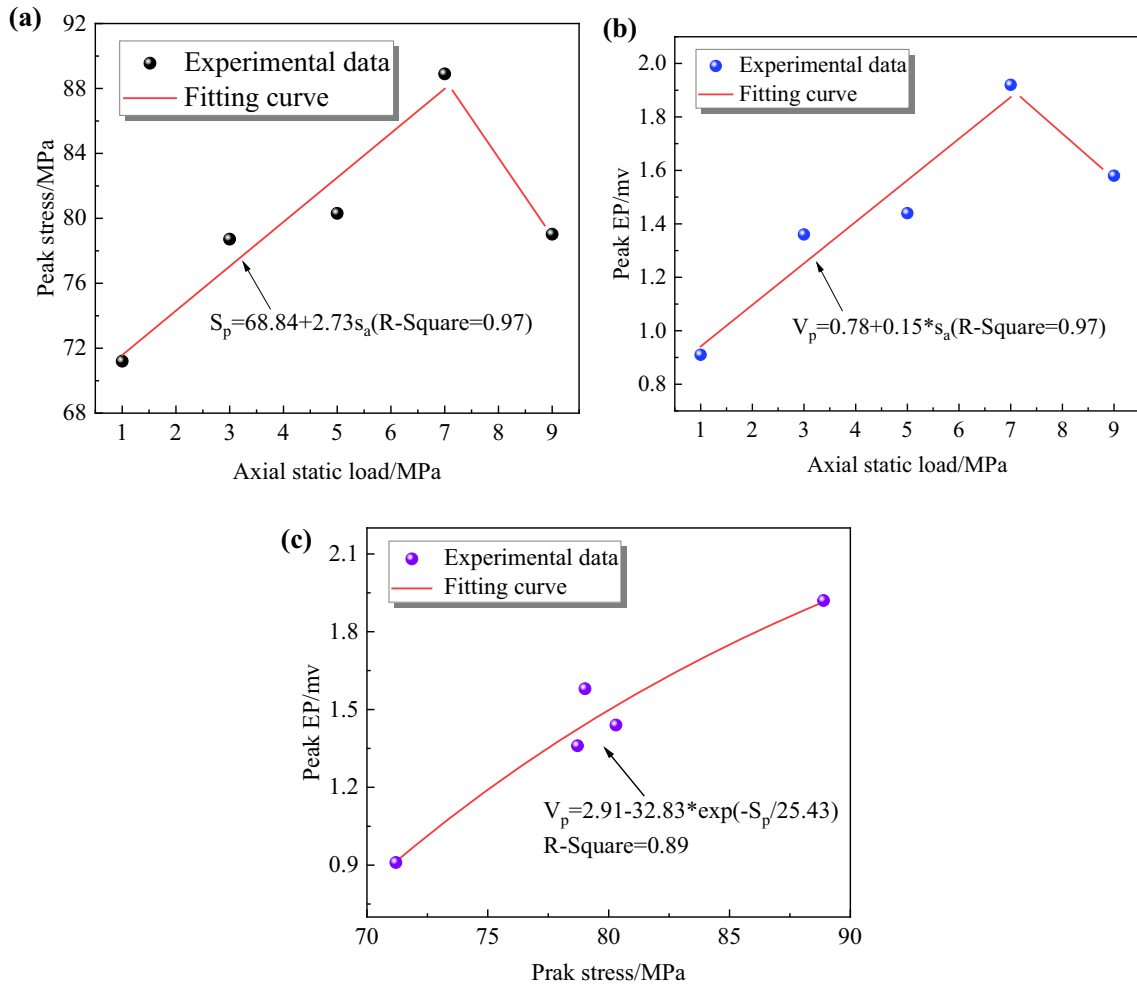where Q_n stands for the normalized accumulated charge, Q_m for the overall accumulated charge, and

(a)

$S_p=68.84+2.73s_a$(R-Square=0.97)

(b)

$V_p=0.78+0.15*s_a$(R-Square=0.97)

(c)

$V_p=2.91-32.83*exp(-S_p/25.43)$
R-Square=0.89

Figure 9. Relation of (**a**) peak stress and (**b**) peak EP to axial static loads, and (**c**) peak EP to peak stress.

Q_i for the initial accumulated charge. Figure 10 depicts the curves of the three changes with time in order to analyze the link between stress level (σ_t/σ_p), strain level ($\varepsilon_t/\varepsilon_p$), and Q_n throughout the sample's failure process, taking sample D-3-1 as an example.

Figure 10 demonstrates that Q_n and the time series change in strain level had a strong correlation. At the initial stage of stress rise (stage I), the internal primary cracks of the specimen were continually closed under dynamic load, and the strain level grew slightly, but the cumulative charge nearly did not change. This was because the coal contained quartz (piezoelectric material). The piezoelectric

mineral deformed under the influence of a dynamic load, producing positive and negative electricity on its surface. Semi-quantitative X-ray diffraction analysis showed that the content of quartz in coal was 20.7%, which meant that the free charge produced by the piezoelectric effect was quite tiny. The specimen then underwent elastic deformation, and the elastic energy kept building up inside the coal sample, showing that the strain started to progressively increase, the growth rate steadily rose, and the cumulative charge climbed linearly during this process. In general, coal has a significant number of dislocations, a two-dimensional crystal defect, and
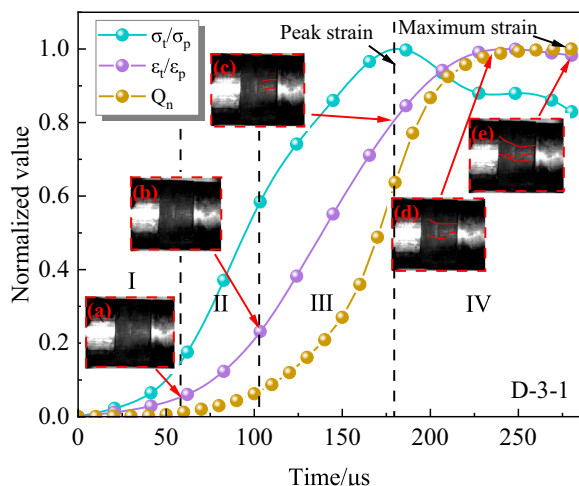
Figure 10. Time series variation of stress level and strain level and normalized accumulated charge of specimen D-3-1.

Figure 11. Variation characteristics of DL at different strain rates.

prior research has revealed that the dislocation region on the surface of coal has a significant potential difference. the surface charge density is highly correlated with the distribution of surface morphology (Tian et al. 2022). A significant number of dislocations are charged and shifted to create local polarization when a coal sample is subjected to elastic deformation. In this procedure, the sample stress and charge density were positively associated. When the stress reached the elastic limit, the sample's internal microcracks gradually began and grew (Fig. 10c). During this process, the strain increased linearly, and the cumulative charge grew exponentially, and the growth rate increased progressively. The cumulative charge growth rate reached its maximum when the stress reached its peak stress. This was so because coal was made up of intricate macromolecular particles that were joined together by intricate atomic interactions, such as covalent bonds, ionic bonds, and hydrogen bonds. In the process of fracture propagation, the stress at the crack tip caused the atomic bond in front to break, and the dangling bonds were produced on the two walls of the new crack, which displayed the same amount of positive and negative electricity, respectively. With the fracture's continued growth, the new crack surface, particularly the crack tip, gathered a significant quantity of free charge, and the accumulated charge increased rapidly, showing that the lo-
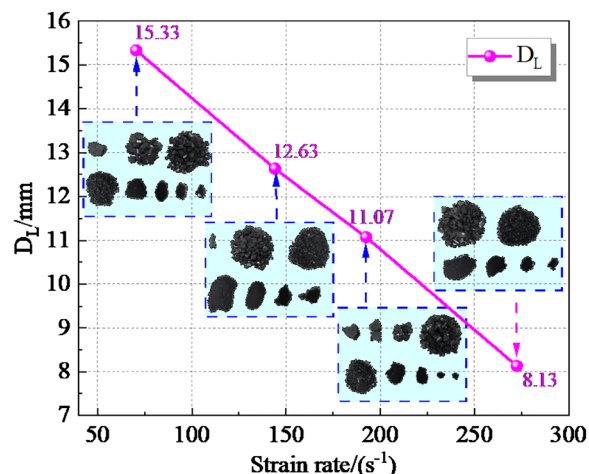
cal EP anomaly became more violent. The strain and cumulative charge continued to increase progressively after the peak stress, but the growth rate gradually slowed down. Figure 10d and e show that the internal cracks of the coal sample were expanding gradually and penetrating, the degree of fracture was increasing progressively, and the corresponding cumulative charge was also increasing gradually. However, as the crack spread, the intensity of the freshmen crack propagation decreased gradually and the corresponding newly generated free charge also decreased gradually as a result of the ongoing release of elastic energy from inside the coal. The pace of growth of the cumulative charge declined gradually. Finally, both the accumulated charge and strain reached their max simultaneously. The sample's fracture process was quite consistent with the changing law of cumulative charge. To verify this viewpoint, we analyzed deeply the impact of various loading situations on the EP response.

Effect of Dynamic and Axial Static Load on EP Response

Effect of Strain Rate on EP Response

In order to quantitatively characterize the degree of fragmentation of the sample, nine sieves of
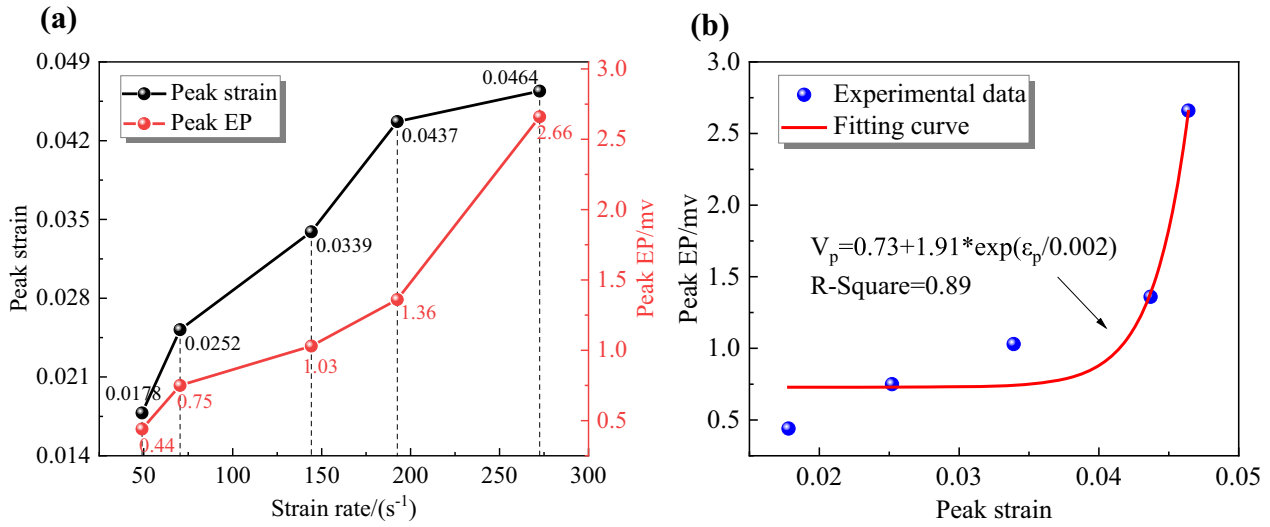
(a)

(b)

Figure 12. (a) Variation characteristics of peak strain and peak EP at different strain rates and (b) fitting curves of the two.

0–0.075, 0.075–0.1, 0.1–0.5, 0.5–1.7, 1.7–7.1, 7.1–22.4, 22.4–31.5, 31.5–45 and > 45 mm were selected to screen the fragments, and the mass of the debris screened by each sieve was weighed by a high-sensitivity electronic scale. In order to represent the level of fragmentation, the average particle size D_L is introduced here. The formula for its calculation is:

$$D_L = \sum_{i=1}^{9} r_i d_i / \sum_{i=1}^{9} r_i \quad (12)$$

where d_i is the average value of the greatest particle size and the minimum particle size in each particle size grade, and r_i is the proportion of the debris mass of each particle size grade to the total mass. Figure 11 shows the variation of the sample's ultimate failure mode and D_L with strain rate. The relationship between peak strain and peak EP and strain rate and the fitting curve of the two are depicted in Figure 12. The figure shows that the peak potential of the coal sample had an exponential growth trend with increase in peak strain. The fitting relationship was:

$$V_p = 0.73 + 1.91 * exp(\varepsilon_p/0.02)(R^2 = 0.89) \quad (13)$$

The figure indicates how the peak strain of the coal sample grew from 0.0178 to 0.0464, the average particle size of the final fragment dropped from

15.33 to 8.13 mm, and the degree of fragmentation increased gradually as the strain rate increased from 49.05 to 272.56 s^{-1}. At the same time, the peak EP stimulated by the coal sample's fracture also increased from 0.44 to 2.66 mv. These demonstrate that the coal fracture was the direct cause of the induced EP response.

The fractal dimension of the crushed debris under different strain rates was calculated by using the statistical method of particle size–mass. Based on the fractal theory, the relationship between the particle size and the mass of the debris is (Fan et al. 2022):

$$M(r)/M = (r/a)^k \quad (14)$$

where M is the total mass of debris, r is the equivalent particle size, namely sieve diameter, $M(r)$ is the mass of debris less than the sieve diameter r, and a is the average size of debris. The logarithm of both sides of Eq. 14 is taken at the same time and the $lg[M(r)/M]$-lgr double logarithmic curve is drawn. The slope k of the fitting curve is obtained by linear fitting, and the fractal dimension D_k of the debris is (Fan et al. 2022):
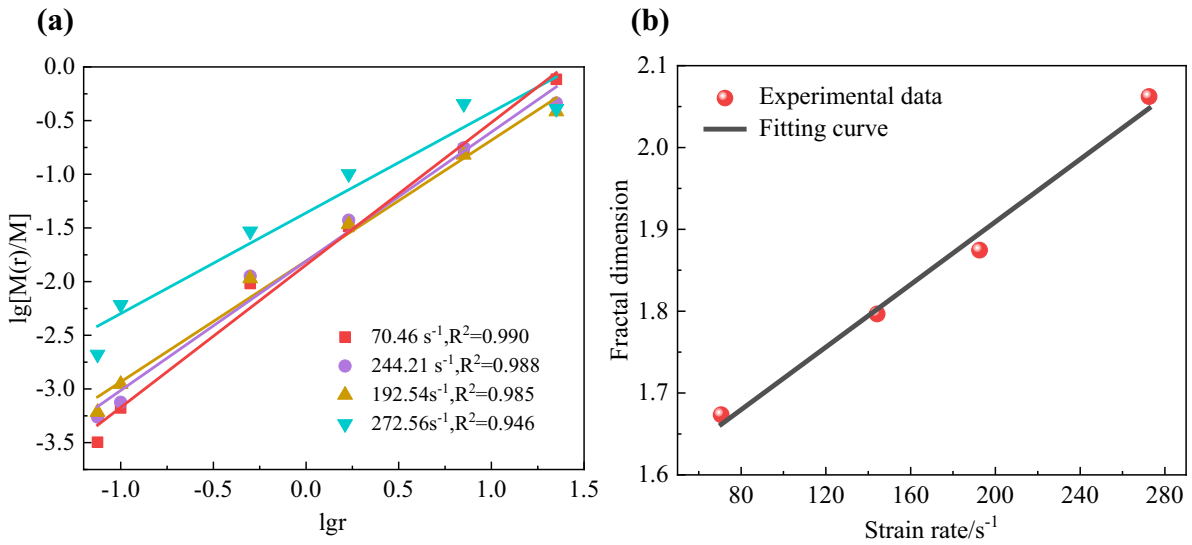
$$D_k = 3 - k \quad (15)$$

Figure 13. Relationship of (**a**) lg$r$–lg[$M(r)/M$] at different strain rates and (**b**) fractal dimension and strain rate.

The value of D_k calculated by this method varies between 0 and 3. When $0 < D_k < 2$, the proportion of large-scale debris is larger; when $D_k = 2$, the proportion of debris mass in each scale is equal; when $2 < D_k < 3$, the proportion of small-scale debris is larger.

The fractal dimension of the fragments under different strain rate conditions was calculated According to the Eqs. 14 and 15 (Fig. 13a), which is the lg$r$–lg[$M(r)/M$] relationship curve under different strain rate conditions. It is shown that there was a good linear relationship between the experimental scatter points in the double logarithmic coordinates, and the correlation coefficients of the calculation results were all greater than 0.94, indicating that the fragmentation distribution of the sample after crushing at different strain rates had significant fractal characteristics. This was because the initiation, propagation and penetration of micro-cracks had a certain self-similarity, and the fracture of the sample was essentially a process of continuous expansion of micro-cracks, which led to the same self-similarity of the distribution of fragments, and so the block distribution was a fractal feature with statistical significance.

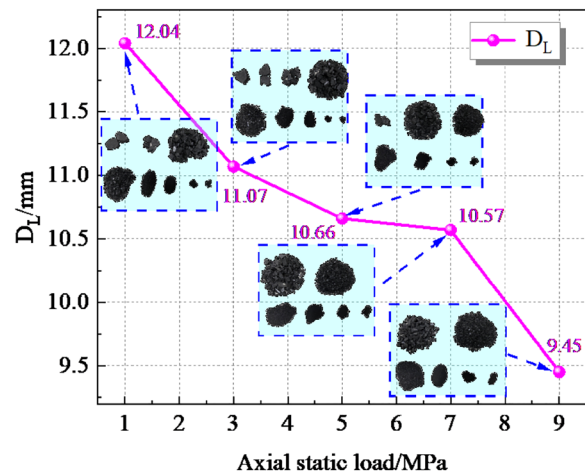Figure 13b shows the relation curve between fractal dimension and strain rates. It shows that the

Figure 14. Variation characteristics of D_L different axial static loads.

fractal dimension of the sample at different strain rates varied between 1.65 and 2.1, and the fractal dimension increased with increase in strain rate. It shows that the proportion of small-scale fragments in the total mass increased gradually, the degree of fragmentation of the sample increased, and the fragmentation decreased gradually. The calculation results were consistent with the above conclusions.
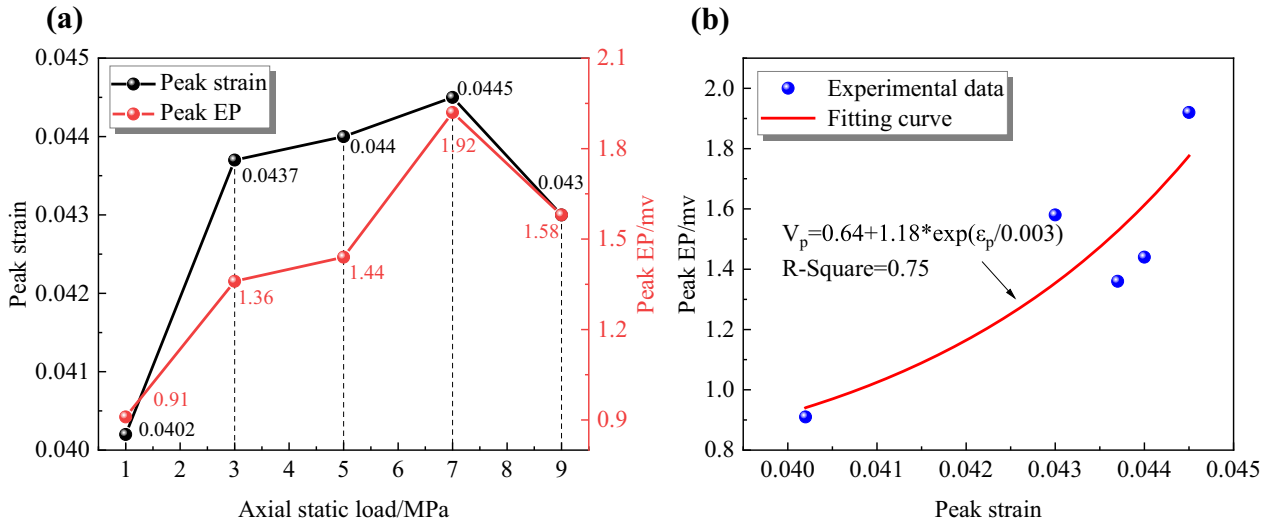
Figure 15. (**a**) Variation characteristics of peak strain and peak EP at different axial static loads and (**b**) fitting curves of the two.

According to the results discussed in section EP Generation of Coal under Dynamic Loading, crack propagation (stage III) was the main reason for the rapid rise of EP signal during the fracture process of coal samples. Under the effect of dynamic load, the coal sample caused microcracks to spread, and the crack tip caused a significant quantity of free charge due to charge separation. At the same time, the two crack surfaces constantly released free charges outward as a result of the sliding and dislocation between them. With gradual increase in dynamic load, the stress wave carried higher energy, so that the crack tip that could not meet the energy required for fracture could obtain enough energy. The microcracks in this part began to initiate, expand and penetrate, and the coal sample showed more abundant failure modes. This promoted the fracture of internal chemical bonds. The charge separation caused the new crack area to accumulate more free charges. The density of free charges continued to increase, showing a stronger EP response.

Effect of Axial Static Load on EP Response

Figure 14 shows the variation of the sample's ultimate failure mode and D_L with axial static load.

The relationship between peak strain and peak EP and axial static load and the fitting curve of the two are depicted in Figure 15. The figure shows that the peak potential of the coal sample also had an exponential growth trend with increase in peak strain. The fitting relationship was:

$$V_p = 0.64 + 1.18 * \exp(\varepsilon_p/0.03)\left(R^2 = 0.75\right) \quad (16)$$

Figure 15 demonstrates how the peak strain of the coal sample increased from 0.0402 to 0.0445 when the axial static load rose from 1 to 7 MPa. The peak strain of the coal sample started to decline, from 0.0445 to 0.043, as the axial load continued to rise to 9 MPa. The sample's average particle size reduced from 12.04 to 9.45 mm, and its fragmentation continued to rise. The peak EP stimulated by the coal sample's fracture first climbed from 0.91 to 1.92 mv, then fell to 1.58 mv, and the axial static load's inflection point was also 7 MPa. The fractal dimension of the broken debris of the sample under different axial static load conditions was calculated, and the calculation results are shown in Figure 16. The fractal dimension of the samples under different axial static loads varied between 1.75 and 2.25, and it increased gradually with increase in axial static load. This shows that the proportion of small-scale fragments in the total mass increased gradually, the
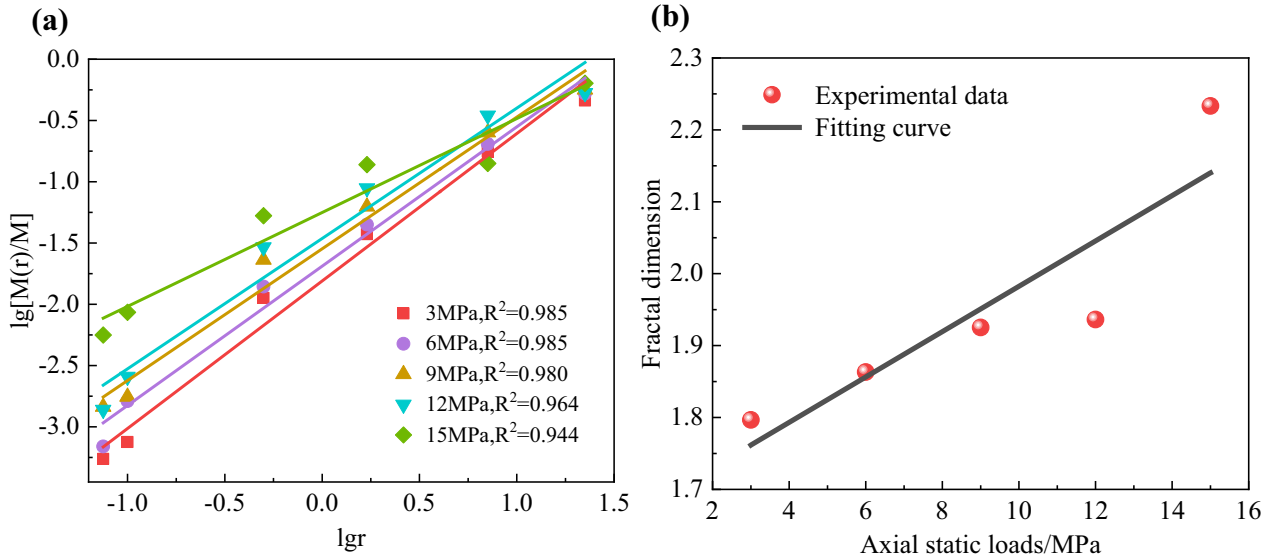
Figure 16. Relationship of (**a**) lg$r$–lg[$M(r)/M$] at different axial static loads and (**b**) fractal dimension and axial static loads.

degree of fragmentation of the sample increased, and the fragmentation decreased gradually. The calculation results were consistent with the above conclusions. It is worth mentioning that when the axial pressure increased to 9 MPa, the crushing degree of coal samples continued to increase, but the peak EP decreased. Although it appears that this analysis was different from the one before, it was not in conflict with it.

In fact, coal fracture and deformation are both processes of energy conversion. Coal will first generate stress concentration near the crack tip when subjected to an axial static load. The fracture tip acquires extraordinarily high elastic strain energy due to the localized high stress, with a level of energy as high as 10^3–10^4 (Guo et al. 1989). In quantum mechanics theory (Li et al. 2022), it is believed that electrons outside the atomic nucleus will move at a high speed on their respective energy level orbits. As soon as the electrons in the atom get energy, they go through an energy level transition and start to gradually drift away from the intra-nuclear protons. Dynamic load causes the electrons in atoms to gain sufficient energy to separate from the intranuclear protons and become free electrons that can escape outward. Consequently, free charge continues to accumulate. As the axial static load rises gradually,

coal deforms to a greater extent, the crack tip builds up more elastic energy. After obtaining higher energy, the degree of deviation of electrons from protons in the nucleus gradually increases. Under dynamic load carrying the same energy, it is easier for electrons to escape and release more free charges, resulting in a significant increase in local charge density. Micro-cracks start to form inside the coal sample when the axial static load goes above a critical value. Prior to the dynamic load acting on a coal sample, its local area experiences free charge escape, and the elastic energy of the corresponding part is also released. Therefore, the coal sample exhibited a continuous increase in the degree of fragmentation under the same dynamic load, but its peak strain and peak EP started to decline. The EP response law and the intensity of coal sample rupture were highly consistent.

Damage Constitutive Model Based on EP Characterization

Definition of Damage Variables

An EP signal, a macroscopic physical phenomenon, is brought on by a charge anomaly during

deformation and fracture of coal. Assuming that the destruction of each micro-unit is accompanied by EP signal generation, there is positive correlation between the damage parameters of coal and the EP. On the basis of this, the coal damage calculation formula is established. Coal is assumed to be homogeneous and isotropic, its obey Hooke's law before destruction, and it follows the Weibull distribution for micro-unit strength. Because of the latter (Fu et al. 2013; Wang et al. 2019; Xiao et al. 2020; Jiang et al. 2022), the probability density function is:

$$P(F) = \begin{cases} \dfrac{m_0}{F_0}\left(\dfrac{F}{F_0}\right)^{m-1} \exp\left[-\left(\dfrac{F}{F_0}\right)^m\right] & (F > 0) \\ 0 & (F \leq 0) \end{cases}$$

(17)

where F is the distribution variable of the micro-unit strength m_0; m and F_0 are the characterization parameters of Weibull distribution. The damage of each micro-unit is a gradual process. In order to reflect this process, the damage variable is introduced here on the basis of Weibull distribution (Liu et al. 2011), and its expression is:

$$D = \frac{N_f}{N}$$

(18)

where D is the statistical damage variable, N_f is the number of damaged micro-units, and N is the total number of micro-units. In any interval $[F, F + dF]$, the number of damaged micro-elements is set to $NP(x)dx$. The number of damaged micro-elements when the external load reaches F is:

$$N_f(F) = \int_0^F NP(x)dx = N\left\{1 - \exp\left[-\left(\frac{F}{F_0}\right)^m\right]\right\}$$

(19)

Equation 19 can be substituted with Eq. 18 to get:

$$D = 1 - \exp\left[-\left(\frac{F}{F_0}\right)^m\right]$$

(20)

Micro-Units' Strength

Equation 20 demonstrates that the strength F of the micro-units has an impact on the damage variable D, and that this strength changes as the micro-unit's stress state changes. The Druck–Prager (D–P) failure criterion is introduced here in order to take the effect of the stress state on coal into consideration. The criterion has the properties of simple parameters and suitable for coal rock for coal rock. Therefore, according to the D–P failure criterion, the micro-unit strength is:

$$F = f(\sigma) = \alpha_0 I_1 + \sqrt{J_2}$$

(21)

where $f(\sigma)$ is the failure criterion, α_0 is the strength parameter of the micro-units, I_1 is the first stress invariant, and J_2 is the second stress deviator invariant. According to D–P failure criterion:

$$\alpha_0 = \frac{\sin\varphi}{\sqrt{3(3 + \sin^2\varphi)}}$$

(22)

$$I_1 = \sigma_1' + \sigma_2' + \sigma_3'$$

(23)

$$J_2 = \frac{1}{6}\left[(\sigma_1' - \sigma_2')^2 + (\sigma_2' - \sigma_3')^2 + (\sigma_3' - \sigma_1')^2\right]$$

(24)

where φ is the internal friction angle; σ_1', σ_2', σ_3' are effective stresses, and their nominal stresses are σ_1, σ_2, σ_3, respectively. The damage body of a coal sample effectively expresses stress as:

$$\sigma_1' = \sigma_i/(1 - D)(i = 1, 2, 3)$$

(25)

Establishment of Damage Constitutive Model

The coal sample in this experiment was also put under prestress from an axial static load while being affected by a dynamic load. Therefore, both axial dynamic load and axial static load were included in the axial stress (Wang et al. 2019), thus:
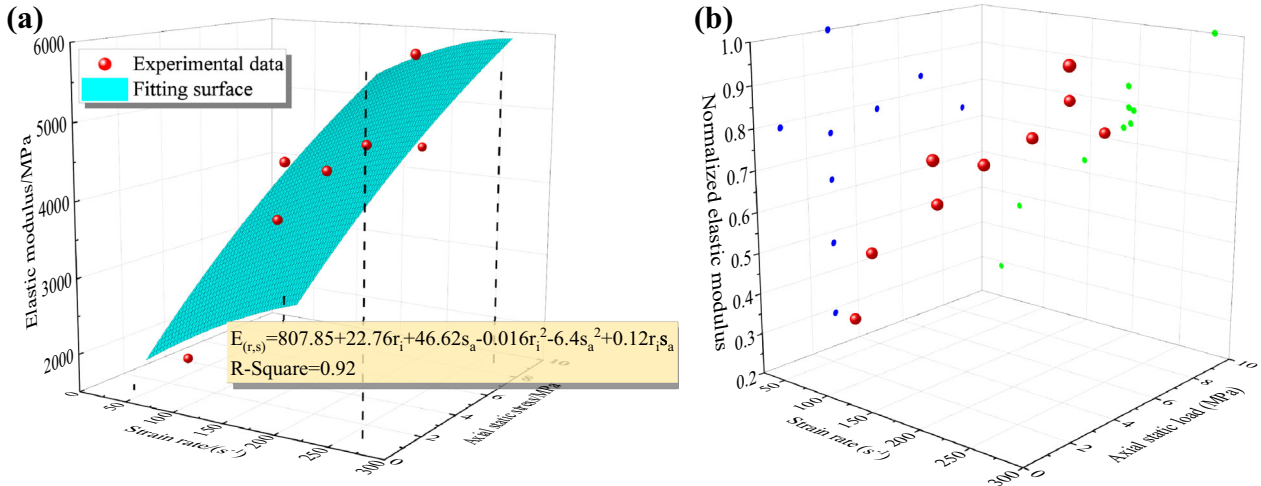
$$\sigma_1 = \sigma_d + \sigma_s$$

(26)

Figure 17. The fitting surface of elastic modulus to strain rate and axial static load..

where σ_1 is axial stress, σ_d is dynamic load stress, and σ_s is static load prestress. According to Hooke's law, the axial strain expression for a coal sample is:

$$\varepsilon_1 = \frac{1}{E}\left(\sigma_1' - v\sigma_2' - v\sigma_3'\right) \tag{27}$$

where ε_1 is axial strain, and v is Poisson's ratio. Because just the axial static load part was present in this experiment, $\sigma_2 = \sigma_3 = 0$, Eq. 21 can be reduced to:

$$\varepsilon_1 = \frac{1}{E}\sigma_1' \tag{28}$$

Equation 25 is introduced into Eq. 28 to obtain:

$$\varepsilon_1 = \frac{1}{E}\left[\frac{\sigma_1}{(1-D)}\right] \tag{29}$$

Therefore, the coal's damage constitutive relation expression for both dynamic and static loads is:

$$\sigma_1 = E(1-D)\varepsilon_1 \tag{30}$$

The damage and EP of coal deformation and fracture share the same statistical distribution law, as can be observed from the previous description. Consequently, when the coal sample strain is ε, the cumulative EP value can be represented as:

$$V = V_m \int_0^F P(x)dx \tag{31}$$

where V_m is the cumulative EP value of the whole process of coal sample failure. Integrating both sides of Eq. 31, we get:

$$\frac{V}{V_m} = 1 - \exp\left[-\left(\frac{F}{F_0}\right)^c\right] \tag{32}$$

Equations 32 and 20 are contrasted, thus:

$$D = \frac{V}{V_m} \tag{33}$$

The expression of the coal damage constitutive relation stated by EP under dynamic and static load is:

$$\sigma_1 = E\left(1 - \frac{V}{V_m}\right)\varepsilon_1 \tag{34}$$

Due to the obvious enhancement effect that dynamic load and axial static load have on the strength of coal sample, coal's strengthening coefficient with respect to them is defined as:

$$G_{(r,s)} = 1 - \frac{E_{(r,s)}}{E_0} \tag{35}$$

where E is the elastic modulus of coal when the strain rate is r_i and the axial static load is s_a; E_0 is the elastic modulus of coal sample D-1-1. The elastic modulus fitting surface under various dynamic and axial static load conditions was obtained in accordance with the experimental data (Fig. 17). The empirical equation is:
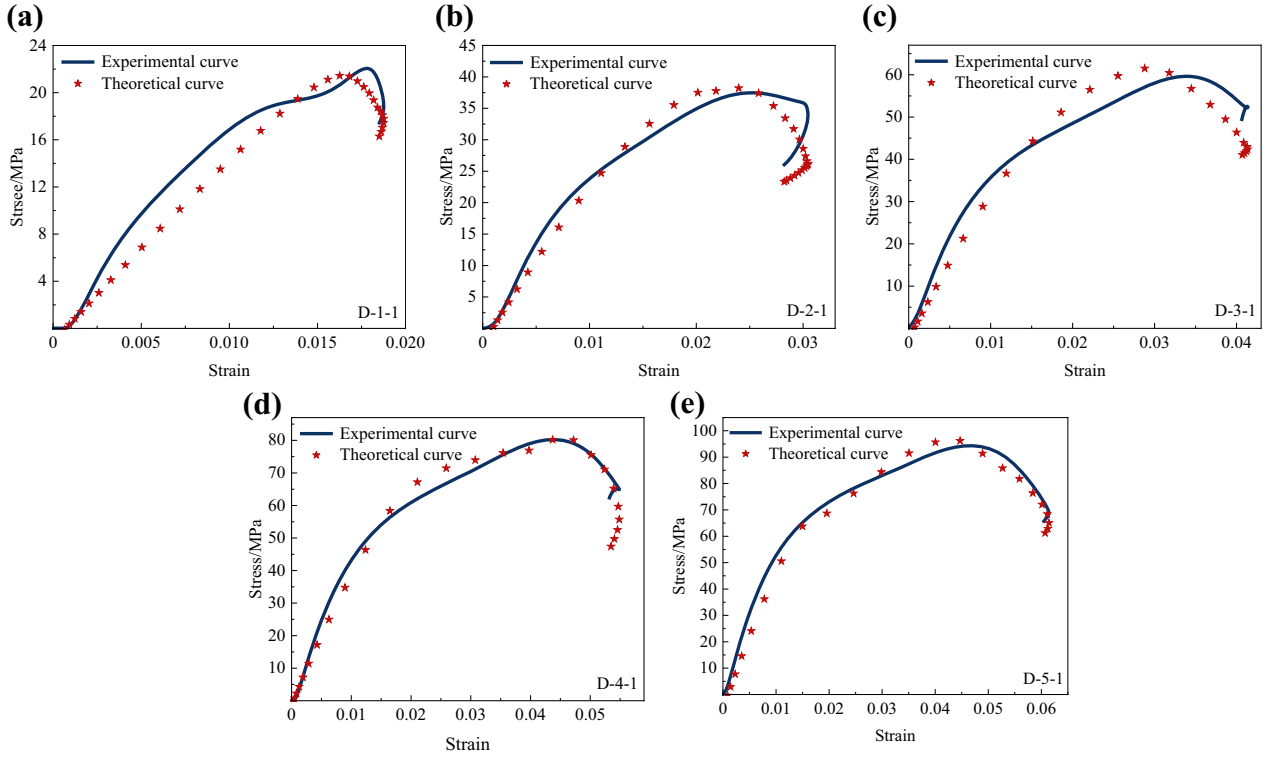
Figure 18. Comparison of the results of theoretical curve and experimental curves of coal samples with different strain rates: (**a**) D-1-1; (**b**) D-2-1; (**c**) D-3-1; (**d**) D-4-1; (**e**) D-5-1.

$$E_{(r,s)} = 807.85 + 22.76r_i + 46.62s_a - 0.016r_i^2 - 6.4s_a^2 + 0.12r_is_a\left(R^2 = 0.92\right)$$

$$(36)$$

where the coal damage constitutive model based on EP characterization can be constructed by combining Eqs. 30, 34 and 35, thus:

$$\sigma_d = \left[1 - G_{(r,s)}\right]E_0\left(1 - \frac{V}{V_m}\right)\varepsilon_1 - \sigma_s \quad (37)$$

Under the condition of full consideration of dynamic and static load coupling, the model can calculate the damage status of coal by EP.

Verification of Damage Configurative Model

The damage constitutive model mentioned above was used to calculate the stress–strain theoretical curves for the coal fracture process, which were then compared to experimental test results (Figs. 18 and 19). These figures show how the theoretical curve's effect to fit gradually better as strain rate rises. This is due to the stress–strain test findings' considerable fluctuations at low strain rates, which will interfere with the calculation results and leads to a rather poor fitting effect. However, there was high agreement between theoretical curves for stress and strain of coal samples under various dynamic and static load circumstances and experimental curves, suggesting that the calculation outcomes of the model may reflect accurately the stress state of coal.

In this work, we used EP response to reveal the dynamic characteristics of coal under axial static–dynamic coupling. The EP testing technology has been used extensively in laboratories and in mining sites as a promising geophysical testing technology. However, testing and analyzing the EP signal under dynamic load still presents significant challenges due to the highly quick loading time and the sample's incredibly complex failure process. Therefore, in future research, we will continue to choose additional types of rock samples for dynamic load experimental research in order to discover the gen-
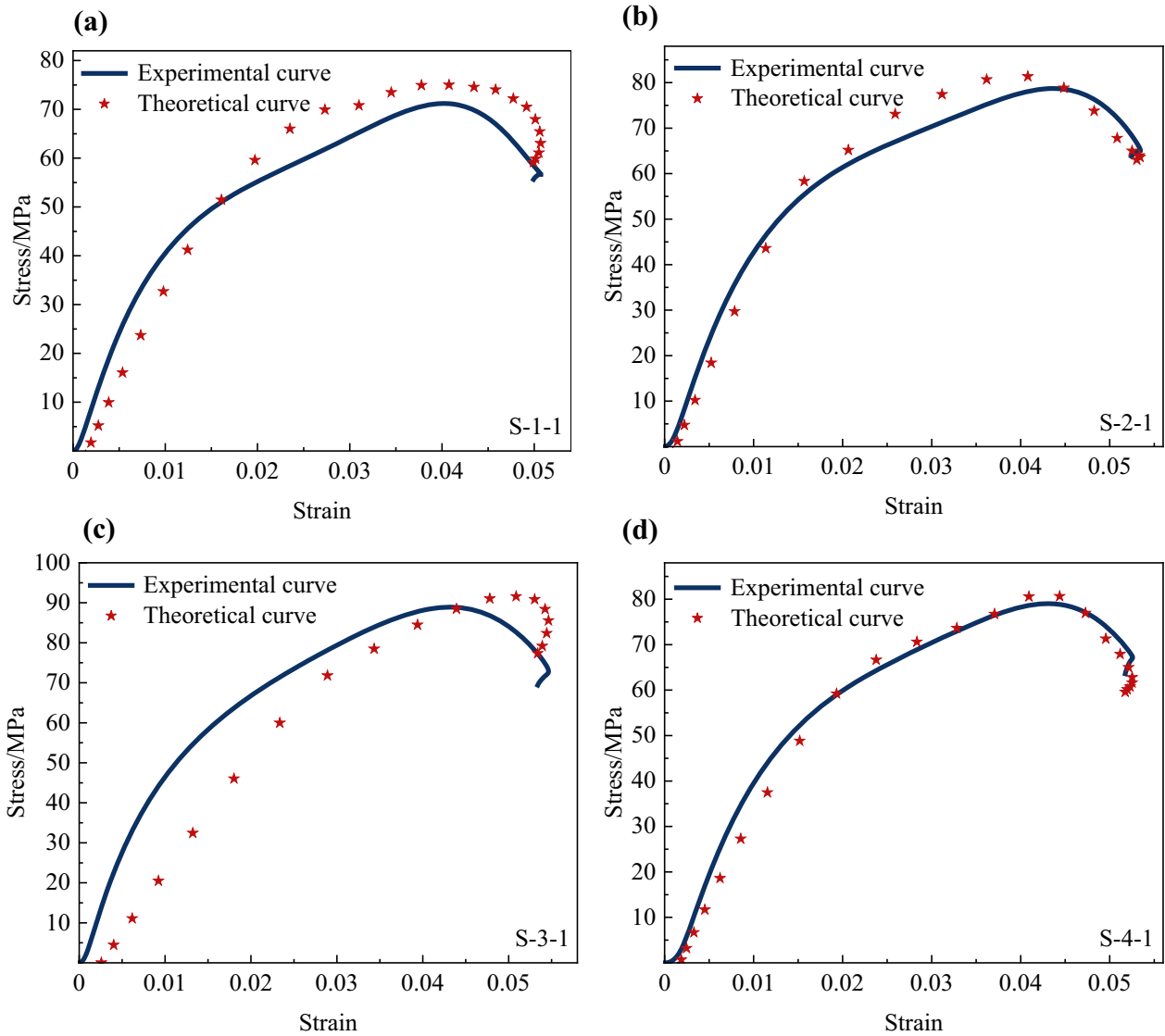
Figure 19. Comparison of the results of theoretical curve and experimental curves of coal samples with different axial static loads: (**a**) S-1-1; (**b**) S-2-1; (**c**) S-3-1; (**d**) S-4-1.

eral law of EP signals generated by these rock samples as well as the differences among them.

CONCLUSIONS

In this paper, the SHPB system was integrated with high-speed camera and EP testing technology. We studied the EP response characteristics of coal under axial static load–dynamic load coupling conditions, and analyzed in detail the impact of various dynamic and static load coupling conditions on EP response. The following main conclusions were reached:

Under axial static load–dynamic load coupling, the EP signal generated by coal has an excellent synchronization with the stress change. However, the growing impact load tends to excite a greater EP signal, and the peak EP rises linearly with dynamic load. The peak EP first grows linearly as the axial static load increases, and peak EP and peak stress start to progressively decline when the peak stress hits the critical value. The law of peak EP varies that is consistent with peak stress.

The free charge produced by coal deformation and fracture mainly comes from the charge separation during crack propagation. However, the progressively increasing dynamic load can produce a higher density of free charges. With increase in axial static load, the continuous accumulation of elastic energy in coal can promote the escape of free electrons and generate more free charges.

We established the EP constitutive model of coal damage evolution under axial static load–dynamic load coupling. Taking into account the combined effect of axial static load–dynamic load, the model forecasts mechanical behavior of coal based on EP signal. The calculation results of this model can be used to determine the stress state of the coal.

ACKNOWLEDGMENTS

DECLARATIONS

Conflict of Interest The authors declared that there is no conflict of interest.

REFERENCES

Cai, M., Kaiser, P. K., Suorineni, F., & Su, K. (2007). A study on the dynamic behavior of the Meuse/Haute-Marne argillite. *Physics and Chemistry of the Earth, Parts A/B/C, 32*(8), 907–916.

Dai, F., Huang, S., Xia, K. W., & Tan, Z. Y. (2010). Some fundamental issues in dynamic compression and tension tests of rocks using split Hopkinson pressure bar. *Rock Mechanics and Rock Engineering, 43*(6), 657–666.

Dai, F., & Xia, K. W. (2013). Laboratory measurements of the rate dependence of the fracture toughness anisotropy of Barre granite. *International Journal of Rock Mechanics and Mining Sciences, 60*, 57–65.

Enomoto, Y., & Hashimoto, H. (1990). Emission of charged particles from indentation fracture of rocks. *Nature, 346*(6285), 641–643.

Fan, W. B., Zhang, J. W., Dong, X. K., Zhang, Y., Yang, Y., Zeng, W. G., & Wang, S. Y. (2022). Fractal dimension and energy-damage evolution of deep-bedded sandstone under one-dimensional dynamic and static combined loading. *Geomechanics and Geophysics for Geo-Energy and Geo-Resources, 8*(6), 1–20.

Feng, X. J., Ding, Z., Ju, Y. Q., Zhang, Q. M., & Ali, M. (2022). "Double peak" of dynamic strengths and acoustic emission responses of coal masses under dynamic loading. *Natural Resources Research, 31*(3), 1705–1720.

Freund, F. (2002). Charge generation and propagation in igneous rocks. *Journal of Geodynamics, 33*(4–5), 543–570.

Freund, F. (2011). Pre-earthquake signals: Underlying physical processes. *Journal of Asian Earth Sciences, 41*(4–5), 383–400.

Fu, Y. K., Xie, B. J., & Wang, Q. F. (2013). Dynamic mechanical constitutive model of the coal. *Journal of China Coal Society, 38*(10), 1769–1774.

Gong, F. Q., Si, X. F., Li, X. B., & Wang, S. Y. (2019). Dynamic triaxial compression tests on sandstone at high strain rates and low confining pressures with split Hopkinson pressure bar. *International Journal of Rock Mechanics and Mining Sciences, 113*, 211–219.

Guo, Z. Q., You, J. H., Li, G., & Shi, X. J. (1989). The model of compressed atoms and electron emission of rock fracture. *Acta Geophysica Sinica, 2*, 173–177.

He, M. C., Ren, F. Q., & Liu, D. Q. (2018). Rockburst mechanism research and its control. *International Journal of Mining Science and Technology, 28*(5), 829–837.

Howe, J. C., & Greb, S. F. (2005). Geologic hazards in coal mining: Prediction and prevention. *International Journal of Coal Geology, 64*(1–2), 1–2.

Ji, D. L., Zhao, H. B., & Vanapalli, S. K. (2023). Damage evolution and failure mechanism of coal sample induced by impact loading under different constraints. *Natural Resources Research, 32*(2), 619–647.

Jiang, H. P., Jiang, A. N., Yang, X. R., & Zhang, F. R. (2022). Experimental investigation and statistical damage constitutive model on layered slate under thermal-mechanical condition. *Natural Resources Research, 31*(1), 443–461.

Jiang, R. C., Dai, F., Liu, Y., & Li, A. (2021). Fast marching method for microseismic source location in cavern-containing rockmass: Performance analysis and engineering application. *Engineering, 7*(7), 1023–1034.

Kenkmann, T., Poelchau, M. H., & Wulf, G. (2014). Structural geology of impact craters. *Journal of Structural Geology, 62*, 156–182.

Kong, X. G., He, D., Liu, X. F., Wang, E. Y., Li, S. G., Liu, T., et al. (2022). Strain characteristics and energy dissipation laws of gas-bearing coal during impact fracture process. *Energy, 242*, 123028.

Kong, X. G., Li, S. G., Wang, E. Y., Ji, P. F., Wang, X., Shuang, H. Q., & Zhou, Y. X. (2021). Dynamics behaviour of gas-bearing coal subjected to SHPB tests. *Composite Structures, 256*, 113088.

Kong, X. G., Wang, E. Y., Li, S. G., Lin, H. F., Zhang, Z. B., & Ju, Y. Q. (2020). Dynamic mechanical characteristics and fracture mechanism of gas-bearing coal based on SHPB experiments. *Theoretical and Applied Fracture Mechanics, 105*, 102395.

Kyriazopoulos, A., Stavrakas, A., Anastasiadis, C., Triantis, D., Biolek, D., & Mastorakis, N. (2005). Pressure stimulated current (PSC) recordings on cement mortar and marble. In Presented at the 4th WSEAS International Conference on Applications of Electrical Engineering (AEE 05) (pp. 12–15).

Leeman, J. R., Scuderi, M. M., Marone, C., Saffer, D. M., & Shinbrot, T. (2014). On the origin and evolution of electrical signals during frictional stick slip in sheared granular material. *Journal of Geophysical Research: Solid Earth, 119*(5), 4253–4268.

Li, C. J., Xu, Y., Chen, P. Y., Li, H. L., & Lou, P. J. (2020a). Dynamic mechanical properties and fragment fractal characteristics of fractured coal–rock-like combined bodies in split Hopkinson pressure bar tests. *Natural Resources Research, 29*(5), 3179–3195.

Li, D. Y., Gao, F. H., & Zhu, Q. Q. (2020b). Experimental evaluation on rock failure mechanism with combined flaws in a connected geometry under coupled static-dynamic loads. *Soil Dynamics and Earthquake Engineering, 132*, 106088.

Li, D. Y., Han, Z. Y., Sun, X. L., Zhou, T., & Li, X. B. (2019a). Dynamic mechanical properties and fracturing behavior of marble specimens containing single and double flaws in SHPB tests. *Rock Mechanics and Rock Engineering, 52*(6), 1623–1643.

Li, D. Y., Han, Z. Y., Zhu, Q. Q., & Ranjith, P. G. (2019b). Stress wave propagation and dynamic behavior of red sandstone with single bonded planar joint at various angles. *International Journal of Rock Mechanics and Mining Sciences, 117*, 162–170.

Li, H. R., Qiao, Y. F., Shen, R. X., He, M. C., Cheng, T., Xiao, Y. M., & Tang, J. (2021a). Effect of water on mechanical behavior and acoustic emission response of sandstone during loading process: phenomenon and mechanism. *Engineering Geology, 294*, 106386.

Li, X. L., Chen, S. J., Liu, S. M., & Li, Z. H. (2021b). AE waveform characteristics of rock mass under uniaxial loading based on Hilbert-Huang transform. *Journal of Central South University, 28*(6), 1843–1856.

Li, X., Li, H., Yang, Z., Zou, H., Sun, W. M., Li, H. Z., & Li, Y. (2022). Coupling mechanism of dissipated energy-infrared radiation energy of the deformation and fracture of composite coal-rock under load. *ACS Omega, 7*(9), 8060–8076.

Li, X. L., Liu, Z. T., Feng, X. J., Zhang, H. J., & Feng, J. J. (2021c). Effects of acid sulfate and chloride ion on the pore structure and mechanical properties of sandstone under dynamic loading. *Rock Mechanics and Rock Engineering, 54*(12), 6105–6121.

Li, X. L., Liu, Z. T., Zhao, E. L., Liu, Y. B., Feng, X. J., & Gu, Z. J. (2023). Experimental study on the damage evolution behavior of coal under dynamic Brazilian splitting tests based on the split Hopkinson pressure bar and the digital image correlation. *Natural Resources Research, 32*(3), 1435–1457.

Li, X. B., Lok, T. S., & Zhao, P. J. (2000). Oscillation elimination in the Hopkinson bar apparatus and resultant complete dynamic stress–strain curves for rocks. *International Journal of Rock Mechanics and Mining Sciences, 37*(7), 1055–1060.

Li, Z. H., Niu, Y., Wang, E. Y., & He, M. (2019c). Study on electrical potential inversion imaging of abnormal stress in mining coal seam. *Environmental Earth Sciences, 78*(8), 1–14.

Li, Z. H., Zhang, X., Wei, Y., & Ali, M. (2021d). Experimental study of electric potential response characteristics of different lithological samples subject to uniaxial loading. *Rock Mechanics and Rock Engineering, 54*(1), 397–408.

Liu, S. M., Li, X. L., Wang, D. K., Wu, M. Y., Yin, G. Z., & Li, M. H. (2020). Mechanical and acoustic emission characteristics of coal at temperature impact. *Natural Resources Research, 29*(3), 1755–1772.

Liu, S. X., Liu, C. W., Han, X. G., & Cao, L. (2011). Weibull distribution parameters of rock strength based on multi-fractal characteristics of rock damage. *Chinese Journal of Geotechnical Engineering, 33*(11), 1786–1791.

Liu, Y., Dai, F., Feng, P., & Xu, N. W. (2018). Mechanical behavior of intermittent jointed rocks under random cyclic compression with different loading parameters. *Soil Dynamics and Earthquake Engineering, 113*, 12–24.

Liu, Y. B., Wang, E. Y., Jiang, C. B., Zhang, D. M., Li, M. H., Yu, B. C., & Zhao, D. (2023). True triaxial experimental study of anisotropic mechanical behavior and permeability evolution of initially fractured coal. *Natural Resources Research, 32*(2), 567–585.

Niu, Y., Wang, C. J., Wang, E. Y., & Li, Z. H. (2019). Experimental study on the damage evolution of gas-bearing coal and its electric potential response. *Rock Mechanics and Rock Engineering, 52*(11), 4589–4604.

Niu, Y., Wang, E. Y., Li, Z. H., Gao, F., Zhang, Z. Z., Li, B. L., & Zhang, X. (2022). Identification of coal and gas outburst-hazardous zones by electric potential inversion during mining process in deep coal seam. *Rock Mechanics and Rock Engineering, 55*(6), 3439–3450.

Padmanabha, V., Schaefer, F., Rae, A., & Kenkmann, T. (2021). Dynamic split tensile strength of basalt, granite, marble and sandstone: Strain rate dependency and Fragmentation. *Rock Mechanics and Rock Engine, 56*(1), 109–128.

Scoville, J., Sornette, J., & Freund, F. T. (2015). Paradox of peroxy defects and positive holes in rocks Part II: Outflow of electric currents from stressed rocks. *Journal of Asian Earth Sciences, 114*, 338–351.

Slifkin, L. (1993). Seismic electric signals from displacement of charged dislocations. *Tectonophysics, 224*(1–3), 149–152.

Stavrakas, I., Triantis, D., Agioutantis, Z., Maurigiannakis, S., Saltas, V., Vallianatos, F., & Clarke, M. (2004). Pressure stimulated currents in rocks and their correlation with mechanical properties. *Natural Hazards and Earth System Sciences, 4*(4), 563–567.

Stergiopoulos, C., Stavrakas, I., Triantis, D., Vallianatos, F., & Stonham, J. (2015). Predicting fracture of mortar beams under three-point bending using non-extensive statistical modeling of electric emissions. *Physica A: Statistical Mechanics and its Applications, 419*, 603–611.

Surkov, V. V., Molchanov, O. A., & Hayakawa, M. (2003). Pre-earthquake ULF electromagnetic perturbations as a result of inductive seismomagnetic phenomena during microfracturing. *Journal of Atmospheric and Solar-Terrestrial Physics, 65*(1), 31–46.

Takeuchi, A., Lau, B. W. S., & Freund, F. T. (2006). Current and surface potential induced by stress-activated positive holes in igneous rocks. *Physics and Chemistry of the Earth, Parts A/B/C, 31*(4–9), 240–247.

Tian, X. H., He, X. Q., Li, Z. L., Majid, K., Liu, H. F., & Qiu, L. M. (2022). AFM characterization of surface mechanical and electrical properties of some common rocks. *International Journal of Mining Science and Technology, 32*(2), 435–445.

Triantis, D., Anastasiadis, C., Vallianatos, F., & Nover, G. (2007). Electric signal emissions during repeated abrupt uniaxial compressional stress steps in amphibolite from KTB drilling. *Natural Hazards and Earth System Sciences, 7*(1), 149–154.

Triantis, D., Stavrakas, I., Anastasiadis, C., Kyriazopoulos, A., & Vallianatos, F. (2006). An analysis of pressure stimulated currents (PSC), in marble samples under mechanical stress. *Physics and Chemistry of the Earth, Parts A/B/C, 31*(4–9), 234–239.

Vallianatos, F., & Triantis, D. (2008). Scaling in pressure stimulated currents related with rock fracture. *Physica A: Statistical Mechanics and its Applications, 387*(19–20), 4940–4946.

Wang, E. Y., Kong, X. G., He, X. Q., Feng, J. J., Ju, Y. Q., & Li, J. D. (2019). Dynamics analysis and damage constitute equation

of triaxial coal mass under impact load. *Journal of China Coal Society, 44*(7), 2049–2056.

Weng, L., Li, X. B., Taheri, A., Wu, Q. H., & Xie, X. F. (2018). Fracture evolution around a cavity in brittle rock under uniaxial compression and coupled static–dynamic loads. *Rock Mechanics and Rock Engineering, 51*(2), 531–545.

Xia, K. W., & Yao, W. (2015). Dynamic rock tests using split Hopkinson (Kolsky) bar system – A review. *Journal of Rock Mechanics and Geotechnical Engineering, 7*(1), 27–59.

Xiao, W. J., Zhang, D. M., Wang, X. J., Yang, H., Wang, X. L., & Wang, C. Y. (2020). Research on microscopic fracture morphology and damage constitutive model of red sandstone under seepage pressure. *Natural Resources Research, 29*(5), 3335–3350.

Yin, S., Li, Z. H., Niu, Y., Qiu, L. M., Sun, Y. H., Cheng, F. Q., & Wei, Y. (2017). Experimental study on the characteristics of potential for coal rock evolution under loading. *Journal of China Coal Society, 42*(S1), 97–103.

Zang, Z. S., Li, Z. H., Niu, Y., Tian, H., Zhang, X., Li, X. L., & Ali, M. (2021). Energy dissipation and electromagnetic radiation response of sandstone samples with a pre-existing crack of various inclinations under an impact load. *Minerals, 11*(12), 1363.

Zhang, H., Zhao, H. B., Li, W. P., Yang, X. L., & Wang, T. (2020). Influence of local frequent dynamic disturbance on microstructure evolution of coal-rock and localization effect. *Natural Resources Research, 29*(6), 3917–3942.

Zhang, Q., Li, X. C., Gao, J. X., Jia, S. Y., & Ye, X. (2022a). Macro- and Meso-damage evolution characteristics of coal using acoustic emission and Keuence testing technique. *Natural Resources Research, 31*(1), 517–534.

Zhang, Q., Liu, Y., Dai, F., & Jiang, R. C. (2022b). Experimental assessment on the fatigue mechanical properties and frac-

turing mechanism of sandstone exposed to freeze-thaw treatment and cyclic uniaxial compression. *Engineering Geology, 306*, 106724.

Zhang, Q. B., & Zhao, J. (2014). A review of dynamic experimental techniques and mechanical behaviour of rock materials. *Rock Mechanics and Rock Engineering, 47*(4), 1411–1478.

Zhang, X., Li, Z. H., Wang, E. Y., Li, B. L., Song, J. J., & Niu, Y. (2021). Experimental investigation of pressure stimulated currents and acoustic emissions from sandstone and gabbro samples subjected to multi-stage uniaxial loading. *Bulletin of Engineering Geology and the Environment, 80*(10), 7683–7700.

Zhou, Y. X., Xia, K., Li, X. B., Li, H. B., Ma, G. W., Zhao, J., et al. (2012). Suggested methods for determining the dynamic strength parameters and mode-I fracture toughness of rock materials. *International Journal of Rock Mechanics and Mining Sciences, 49*, 105–112.

Zhoujie, G., Shen, R., Liu, Z., Zhao, E., Chen, H., Yuan, Z., Chu, X., & Tian, J. (2023). Dynamic characteristics of coal under triaxial constraints based on the split-Hopkinson pressure bar test system. *Natural Resources Research, 32*(2), 587–601. https://doi.org/10.1007/s11053-022-10152-6.